Integrated Project (IP)
Project No. TIP5-CT-2006-031415

Thematic Priority 6:
Sustainable Development,
Global Change and Ecosystems

Recommendation of, and scientific basis for, optimisation of switches & crossings – part 2

INNOTRACK GUIDELINE

Deliverable report D3.1.6

Table of Contents

1. Executive Summary

The objective of INNOTRACK SP3.1 (task 3.1.6 Optimisation) is the development of innovative S&C (Switches & Crossings) designs that allow for increased axle loads and speeds, and at the same time a decreased need for maintenance. The present report provides results from laboratory measurements of different materials used in S&C, and a methodology for the optimisation of material in the switch and crossing panels.

Wear and accumulated plastic deformation are common damage mechanisms in S&C components. Rolling Contact Fatigue (RCF) is another type of damage mechanism that leads to surface cracks on the rails. To predict the overall degradation of S&C components, it is necessary to consider all these three damage mechanisms. A methodology for simulating (predicting) all these mechanisms for a mixed traffic situation in a switch has been developed. The methodology includes: simulation of dynamic vehicle–track interaction considering stochastic variations in input data, simulation of wheel–rail contacts accounting for non-linear material properties and plasticity, and simulation of wear and plastic deformation in the rail during the life of the S&C component. The risk for RCF is assessed using simplified engineering indices.

Three different materials, R350HT, B360 and Mn13, have been laboratory tested regarding tensile strength at different temperatures and strain rates, and fatigue behaviour. The steels were also investigated metallographically, including chemical analyses, hardness and microstructural studies. The results from the laboratory measurements are required for the calibration of the non-linear material model used in the simulation methodology.

Two examples demonstrating the use of the simulation methodology are reported. In the first example, the influence of increased axle load on the degradation of a switch panel (switch rail and stock rail) is studied. In the second example, rail profile degradation of the frog (crossing nose and wing rails) of a turnout at Haste in Germany is investigated. For the latter example, simulation results have been compared with measurements after five weeks of mixed traffic. Good qualitative agreement was found for the damage (profile evolution) of the crossing nose, which validates the simulation methodology. A number of possible parameter investigations can now be performed with the proposed simulation methodology, such as a study of the influence of traffic situation (vehicle type, speed, axle load etc), switch geometry and material of switch components.

The optimisation of geometry and support stiffness in the switch and crossing panels was reported in Deliverable 3.1.5. Field testing and further laboratory testing of new S&C designs will be performed within INNOTRACK SP3. Some tests have started, whereas some are still in the planning phase. To enable an assessment of the influence of the new designs on the long-term degradation of S&C, these field tests will not be finished and reported before the end of INNOTRACK. A report on results from field tests of different crossing designs at test site Haste in Germany will be reported in INNOTRACK Deliverable 3.1.8 (due in December 2010). Results from field tests (Frankfurt and Wirtheim, Germany) of modified stiffness in the switch panel will be reported in INNOTRACK Deliverable 3.1.9 (due in January 2011). Finally, the results from a field test (Eslöv, Sweden) of new S&C designs will be reported in INNOTRACK Deliverable 3.1.10 (due in May 2011).

2. Introduction

The different components of a switch & crossing (S&C, turnout, point) are illustrated in Figure 1 [2.1]. The through and diverging routes are shown. Traffic in the facing move means that traffic is travelling from the switch panel to the crossing panel. Consequently, traffic in the trailing move means traffic travelling in the opposite direction.

Dynamics and damage of S&C are surveyed in the state-of-the-art report by Sällström et al [2.2]. Mathematical modelling, numerical simulation and field testing of dynamic vehicle–track interaction in S&C are treated by Kassa [2.3]. Statistics on the need for maintenance in S&C have been presented by Nissen [2.4].

INNOTRACK Deliverable 3.1.4 contains a validation of the vehicle dynamics simulation models used here and a pre-report on the optimisation of S&C [2.5]. The optimisation of geometry and support stiffness in the switch and crossing panels was treated in INNOTRACK Deliverable 3.1.5 [2.6].

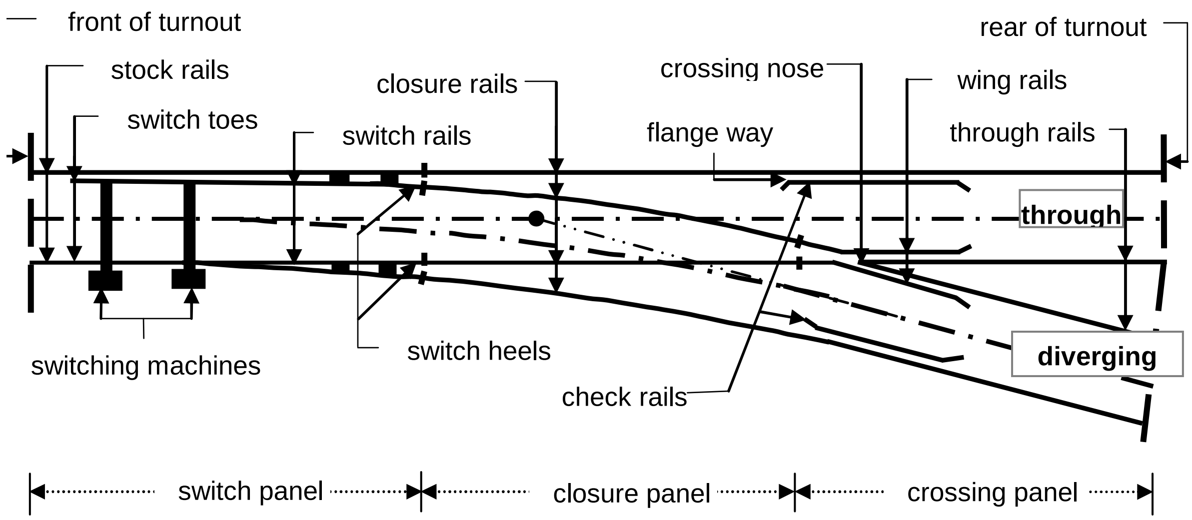

Components of a turnout with through and diverging routes. From [1]

Figure 1

The laboratory tests of materials in switch components, which are summarised here, were performed by Mr Martin Schilke and Dr Johan Ahlström at Chalmers University of Technology (CHARMEC at the Department of Materials and Manufacturing Technology). Section 3 in this guideline was written by Mr Martin Schilke and Dr Johan Ahlström. The methodology for simulation of material degradation and change of rail profiles in S&C was developed by Dr Magnus Ekh, Prof Jens Nielsen, Dr Mats Ander, Mr Jim Brouzoulis, Dr Anders Johansson and Mr Björn Pålsson at Chalmers (CHARMEC at the Department of Applied Mechanics). Section 4 in this guideline was written by Dr Magnus Ekh. The guideline was edited by Prof Jens Nielsen.

2.1. Bibliography

2.1 E Kassa and J C O Nielsen, Dynamic interaction between train and railway turnout – full-scale field test and validation of simulation models. *Vehicle System Dynamics* Vol 46, Issue S1 & 2, 521-534, 2008

2.2 J H Sällström, T Dahlberg, M Ekh and J C O Nielsen, State-of-the art study on railway turnouts – dynamics and damage, Research Report, *Department of Applied Mechanics, Chalmers University of Technology,* Gothenburg, Sweden, 50 pp, 2002

2.3 E Kassa, Dynamic train–turnout interaction – mathematical modelling, numerical simulations and field testing, PhD thesis, *Department of Applied Mechanics, Chalmers University of Technology,* Gothenburg, Sweden, 2007

2.4 A Nissen, Analys av statistic om spårväxlars underhållsbehov (Analysis of statistics on the need for maintenance in switches & crossings, in Swedish), Licentiate Thesis, *Avdelning för drift och underhåll, Luleå Technical University, JvtC – Railway research centre*, Luleå, Sweden, 2005

2.5 J C O Nielsen (editor), Summary of results from simulations and optimisation of switches, INNOTRACK Deliverable 3.1.4, 35 pp and 4 annexes, December 2008

2.6 J C O Nielsen (editor), Recommendations of, and scientific basis for, optimisation of switches and crossings – part 1, INNOTRACK Deliverable 3.1.5, 27 pp and 2 annexes, July 2009

3. Laboratory tests of material properties

3.1. Background

Important material requirements on railway rail steel are to withstand wear and fatigue cracking. The strategy for achieving this has often been to increase the hardness of the used steel alloys. However, the requirements on a crossing nose differ from conventional rail track because of the high impact loads that may occur during the wheel transfer between the wing rail and the crossing nose.

Three different materials have been tested within INNOTRACK regarding tensile strength at different temperatures and strain rates, and regarding fatigue behaviour. Also, the steels were investigated metallographically, including chemical analyses, hardness and microstructural studies.

3.2. Experimental setup

3.2.1. Metallographic examination

Chemical analyses have been performed on the three materials that were supplied by voestalpine Schienen, VAE and Vossloh Cogifer. Samples of each material were ground, polished and etched to reveal the microstructure. Hardness was measured in the area where the samples for fatigue and tensile testing were extracted. These investigations were done to confirm the homogeneity of the sample materials to judge the suitability for subsequent mechanical tests.

3.2.2. Test specimen

Cylindrical specimens according to the sketch in Appendix C were cut out from the rail head parallel to the rolling direction. Specimens for tensile testing were ground down to grit 1200. This removes the deformed surface layers with residual stresses, originating from the machining, and minimises the stress concentrations. All fatigue specimens were further ground and polished down to 1 μm diamond paste to achieve a mirror-like, scratch-free surface in order to minimise the number of fatigue crack initiation sites. This and the adopted testing procedure guarantees a low scatter in fatigue life and makes the results dependent only on the inherent properties of the materials.

3.2.3. Mechanical tests

Two identical tests were performed for almost all different parameter combinations. Tensile tests were conducted with strain rates of 10^{-1} s^{-1} and 10^{-4} s^{-1} at three different temperatures: -60, 20 and 100 °C. Fatigue tests were performed in symmetric strain control (strain ratio $R_\varepsilon = \varepsilon_{\min} / \varepsilon_{\max} = -1$) at constant strain amplitudes of 0.4 %, 0.6 % and 1.0 %. Stress controlled fatigue tests were performed at stress amplitudes equivalent to the stresses achieved in the corresponding strain controlled tests, both with and without a tensile mean stress (stress ratios $R_\sigma = \sigma_{\min} / \sigma_{\max}$ = -1 and -0.8, respectively).

3.2.4. Tested materials

The studied materials were the bainitic B360 and the austenitic Mn13 steel grades. The fine-pearlitic 350HT steel grade was examined within a parallel research project at Chalmers and these results are also included in this report by courtesy of voestalpine Schienen GmbH. For comparison, results from previous research projects at CHARMEC on the standard pearlitic R260 steel grade are included in some graphs [3.1].

3.3. Results

3.3.1. Metallographic examination and hardness tests

The microstructural investigations of cross sectioned rail heads show that the materials are rather homogeneous with respect to grain sizes and carbide/oxide distributions. Table 1 shows the most important alloying elements. For a more complete table, see [3.1].

Hardness tests for B360 and 350HT revealed a uniform hardness distribution throughout the rail heads. The rolled Mn13 showed large gradients in hardness which could derive from deformation hardening during production or from segregation. If the hardness gradients are due to deformation, possible differences between different test bar individuals should even out early during fatigue testing as Mn13 hardens considerably initially. If the hardness gradients are caused by segregation, large scatter could be expected in the LCF results.

Concluding the microstructural and hardness studies, the specimens were judged to give a representative picture of the material behaviour in the rail head for all three studied materials.

Table 1 Shortened list of chemical composition [wt-%]

	C	Cr	Si	Mn	Fe
B360	0.32	0.55	1.27	1.57	96.0
350HT	0.79	0.08	0.44	1.19	97.4
Mn13	1.14	0.18	0.36	12.25	85.8
R260	0.73	0.03	0.32	1.0	97.8

3.3.2. Mechanical tests

An ordering of the materials from a tensile strength point of view gives in descending order first B360 followed by 350HT and R260. Mn13 has the lowest tensile strength but the highest elongation to rupture. This is partly due to the ability of Mn13 to distribute the strain over the tested volume, i.e. to avoid strain localisation to a “necking zone”.

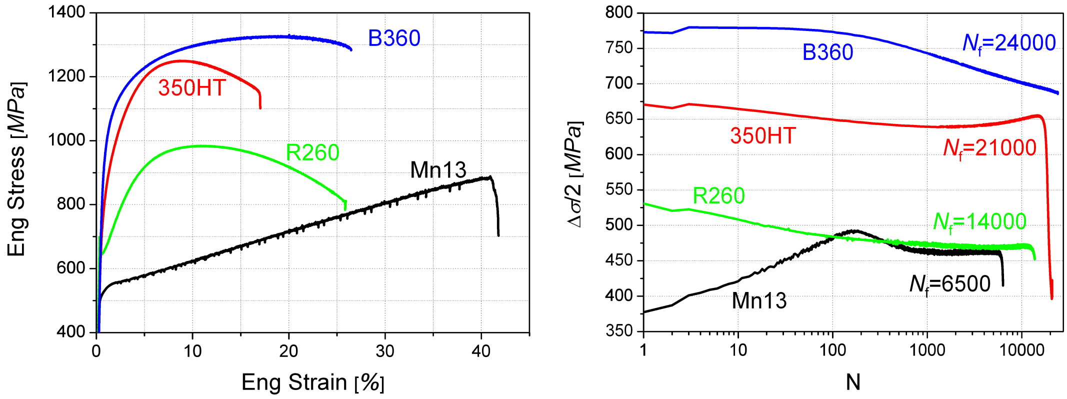

Figure 2. Tensile characteristics at room temperature with a strain rate of 10^{-4} s^{-1} (left). Stress amplitude development from fatigue tests at 0.4 % total strain amplitude (right)

The constant strain amplitude fatigue tests gives the cyclic plastic deformation behaviour of the steels, see Figure 2. The pearlitic R260 and 350HT soften slightly initially, especially at lower strain amplitudes, but harden somewhat during the main part of their life. The bainitic B360 softens continuously during the life, while the austenitic Mn13 shows distinct hardening initially followed by moderate softening. The stress controlled results for each material gives consistent results, except for the Mn13 which hardens much faster under stress amplitude control due to large plastic straining in the first few cycles.

The Wöhler chart, see Figure 3, shows that B360 and 350HT have a substantially longer LCF life than Mn13 and R260 for any given stress amplitude level. The Coffin-Manson diagram represents the LCF life after cycling at a given plastic strain amplitude and is important for judging material behaviour in displacement controlled loading situations. It reveals that B360, 350HT and R260 all have similar slopes and, in the order mentioned, an increasing number of cycles to failure. The austenitic Mn13 has a lower slope and endures fatigue loading at low plastic amplitudes well.

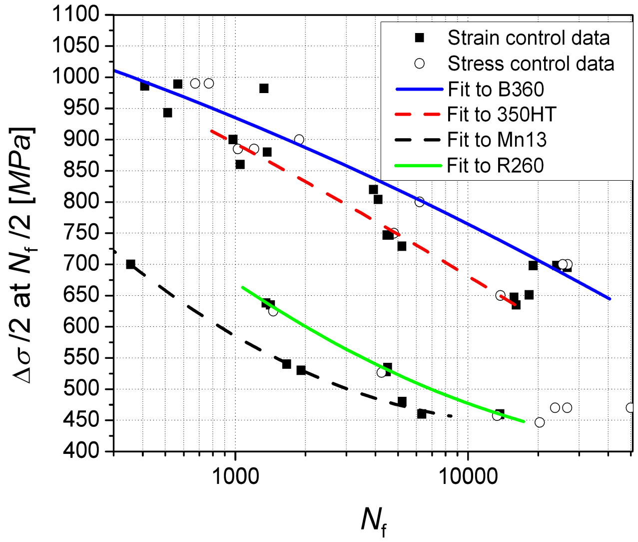

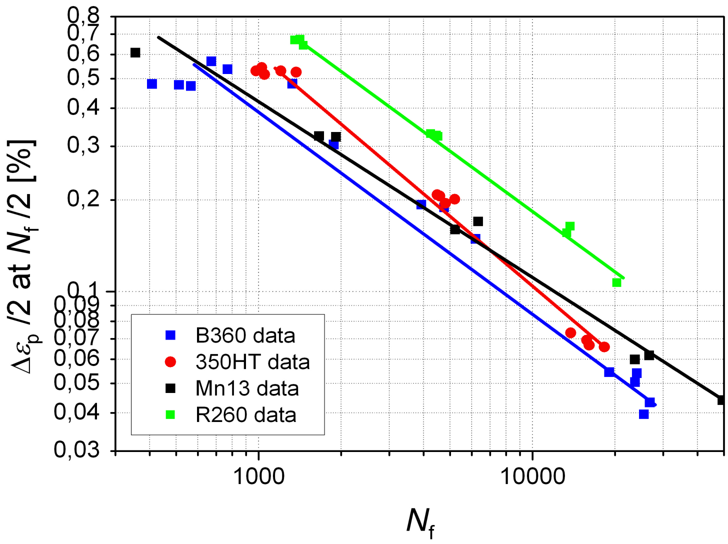

Figure 3. Wöhler chart showing stress amplitude versus number of cycles to failure N_f, with trend lines fitted to strain controlled data, (upper graph) and Coffin-Manson chart with plastic strain amplitude plotted versus number of cycles to failure N_f (lower graph)

3.4. Conclusions and recommendations

The performed tests show correlation between hardness, tensile strength and low cycle fatigue (LCF) life. Thus, the bainitic steel B360 performs best during low cycle fatigue testing, followed by 350HT, R260 and Mn13. This is not consistent with field experience for the Mn13 steel, but there are several differences that can explain this discrepancy:

1. During low cycle fatigue testing in the laboratory, materials are exposed to loads that are cycled around a mean level close to

zero. This means the specimens are exposed to high tensile stresses. In field, the loading is mainly compressive. As the Mn13 steel is difficult to produce without carbide formation in the grain boundaries, these weaker parts of the material will be sensitive to tensile stresses.

2. Due to the repeated loading in field, the material close to the top of the rail head becomes strongly deformed. The high straining leads both to an exhausted ductility and to an aligned structure with weaker planes in the pearlitic grades [3.2], which is not probable in the single phase austenitic Mn13.

3. In field, impact loads with high magnitudes are generated. In low cycle fatigue testing, tests are done with a constant load or strain amplitude, and with a constant strain rate several orders of magnitude lower than in field. It is well known that non-austenitic materials are more sensitive to higher strain rate and lower temperature than austenitic steels.

Despite the inability of the LCF tests to be directly applicable to estimate the life of a material in field (especially for the Mn13 material), the test results are still very valuable. The performed LCF tests provide input material data for calibration of advanced material models describing cyclic plasticity used in subsequent simulations. Further they give a good physical understanding of the behaviour of the different materials in the examined load situation. However, it is recommended to perform additional tests in full-scale test rigs to make life estimates and to identify other material properties that are crucial for a long life in crossing applications.

3.5. Bibliography

3.1 J. Ahlström and B. Karlsson, Fatigue behaviour of rail steel - a comparison between strain and stress controlled loading. *Wear* 258(7-8), 1187-1336, 2005

3.2 A. Hohenwarter, R. Stock and R. Pippan, Changes in the fracture toughness of a rail steel subjected to high pressure torsion. Proceedings of the 12th International Conference on Fracture, Ottawa, Canada, July 12 – 17, 2009

4. Optimisation of material in the switch and crossing panels

4.1. Background

Wear and accumulated plastic deformation are common damage mechanisms in S&C components. In the severe case of a highly worn switch rail, a wheel flange may climb the switch rail resulting in a vehicle derailment. Rolling Contact Fatigue (RCF) is another type of damage mechanism that leads to surface cracks on the rails, which may propagate and cause rail breaks. To predict the overall degradation of S&C components, it is necessary to consider all three damage mechanisms: plastic deformation, wear and RCF. A methodology for simulating (predicting) all these mechanisms for a mixed traffic situation in a switch has been developed. The methodology is presented and demonstrated below.

4.2. Simulation methodology

The methodology for predicting damage of S&C components involves an integration of several cross-disciplinary numerical tools, see Figure 4. For a given S&C design (curve radius, crossing angle, steel grade, etc) with a nominal (or initial) set of rail profiles, the methodology includes the following four steps, see also [4.1]:

I. Vehicle dynamics simulations to calculate wheel–rail contact forces, creepages and contact positions. The influence of stochastic variations in vehicle loads (due to e.g. wheel profile, vehicle type, vehicle speed and wheel position at switch entry) is considered by repeating the dynamic simulation with different sets of vehicle input data.

II. Wheel–rail contact simulations for each load cycle to determine non-Hertzian wheel–rail contact patches taking into account the elasto-plastic material behaviour. The modelling of nonlinear material behaviour is particularly important for S&C applications, where the contact pressures may be high due to severe dynamic loads and/or small contact patches. For each contact position, the outputs to the next step of the methodology are the contact patch size, the maximum von Mises equivalent stress and the maximum contact pressure.

IIIa. Two-dimensional finite element simulations for a large number of load cycles to predict the irreversible plastic deformations and work hardening of the material at rail cross-sections with severe contact loads. The adopted rail material model is based on a formulation for hyper-elastoplasticity that has been calibrated using uni-axial tests with cyclic loading (see Section 3). Results from the contact simulations (step II) and the slip, contact positions and contact forces determined by the simulations of vehicle dynamics (step I) are used as input.

IIIb. Wear simulations at rail cross-sections with severe contact loads using FASTSIM and the Archard wear model. Based on FASTSIM, the contact patch is discretised into a grid.

IV. Updating of rail profiles. The predicted profile of each studied rail cross-section after the load cycles have been applied is obtained by adding the calculated profile changes due to plastic deformation and wear. A smoothing process is then conducted based on calculations of a moving average.

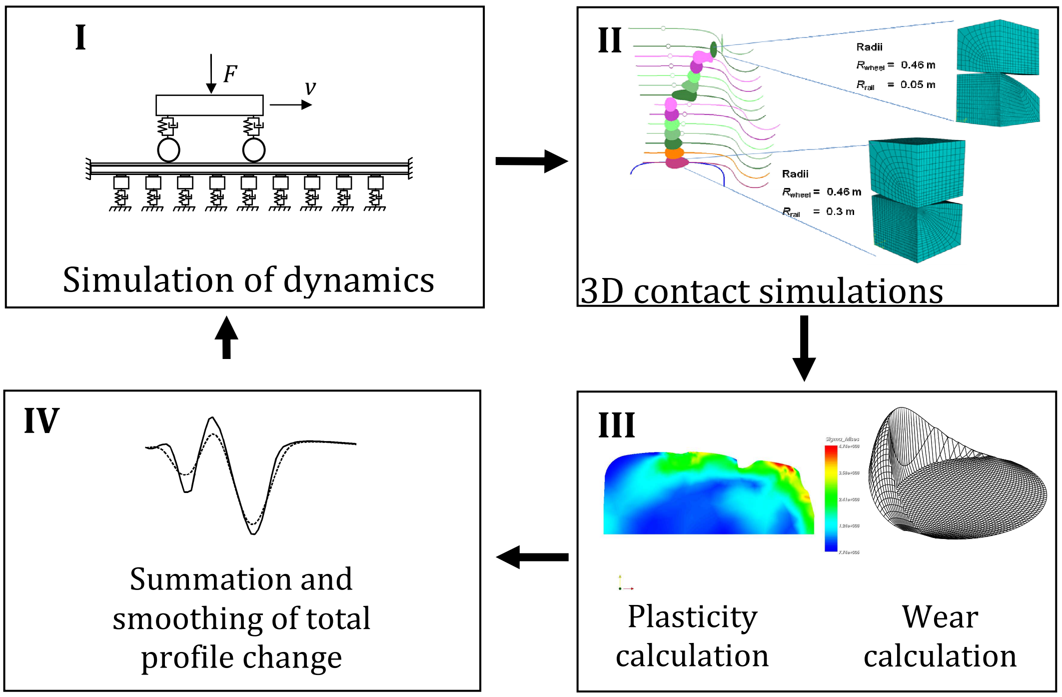

Figure 4. Methodology for simulation of wheel–rail contact and damage in S&C: (I) simulation of dynamic wheel–rail contact forces, (II) calculation of contact stresses, contact patch sizes and contact pressure, (III) simulation of plastic deformation and wear and (IV), summation and smoothing of profile change. From [4.2]

The new set of rail profiles are then used in simulations of vehicle dynamics with the same sets of stochastic vehicle input data. By performing the different steps in an iteration scheme, the gradual development of damage in the S&C components can be simulated for a given number of load cycles.

To obtain accurate predictions of wheel–rail contact stresses (step II) and plastic strains (step IIIa) in S&C components, a calibrated material model of the rail steel is required. In general, it is difficult or even impossible to perform laboratory tests where the specimens are subjected to similar loading situations as for an in-field S&C component. Due to this difficulty, the calibrations of the material model have in this project been based on results from cyclic stress-controlled experiments on uni-axial tensile bars, see Section 3.

4.3. Simulation results

Two demonstration examples of the use of the simulation methodology for calculation of rail profile degradation are presented: the switch panel of a turnout at Härad in Sweden [4.1], and the frog (crossing nose and wing rails) of a turnout at Haste in Germany [4.2].

The Härad turnout is a standard (right turn) design UIC60-760-1:15 (with curve radius 760 m and turnout angle 1:15). The nominal variation of the rail profile (at 40 positions) in the switch panel was measured by MiniProf with sampling distance in the order of 30 cm. The employed freight vehicle model included two Y25 bogies. A representative traffic situation was given as input with Gaussian (normal) probability distributions for train speed v and friction coefficient μ. This together with 18 different wheel profiles (equal probability) gave, using Latin Hypercube sampling, a total of 92 load cases in a representative load sequence. Based on the results from the simulations of dynamic vehicle–track interaction using the computer program GENSYS, two critical rail cross-sections were identified: rail section 24 with the highest wear index [4.1] and rail section 36 with the highest vertical contact force. For rail section 24, wear and plastic deformation gave similar amounts of cross-section degradation. However, for rail section 36 the plastic deformation was the dominating damage mechanism. Increasing the axle load from 25 tonnes to 30 tonnes resulted in an increase of the vertical profile change by 27 %, see Figure 5, whereas the numerical value of the RCF criterion [4.1] was increased by 10 % for rail section 24.

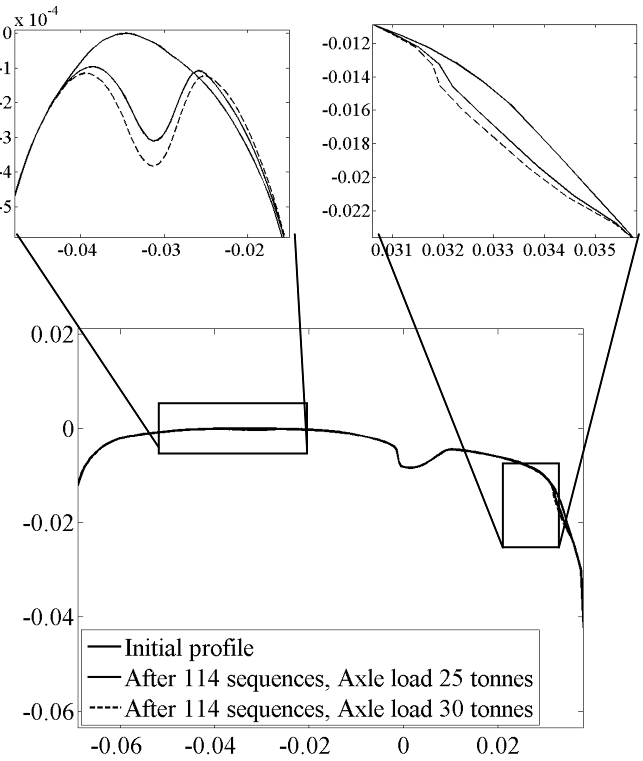

Figure 5. Degradation of rail section 24 of the Härad turnout after 114 load sequences due to wear and plastic deformation, two different axle loads. From [4.1]

The turnout at Haste was studied in a second demonstration example. It is a standard S&C design EH 60-500-1:12 subjected to traffic in the facing move. The dynamic vehicle–track interaction was simulated in the multibody dynamics code SIMPACK. The complete three-dimensional vehicle models of a Loco BR 101 and an ICE-T coach (BR 411), representing two different static wheel loads (107 kN and 67 kN, respectively), were used. A load sequence was designed using Latin Hypercube sampling taking into account four vehicle input variables: wheel profile, lateral wheel position at crossing entry, vehicle speed and vehicle type. The rail profile change of the frog (crossing nose and wing rails) made of R350HT steel was simulated for nine cross-sections. Good qualitative agreement was observed between the simulated and measured rail profile change after five weeks of mixed traffic, corresponding to 200 000 load cycles (or 500 representative load sequences), see Figure 6. More specifically, the largest degradations were found for similar longitudinal positions along the crossing nose (approximately 300 mm away from the tip of the crossing nose), and the simulated and measured profile changes were found to be in the same order of magnitude (approximately 0.5 mm). Plastic deformation was observed to be the dominating degradation mechanism in the beginning, while wear dominated at the end of the degradation process.

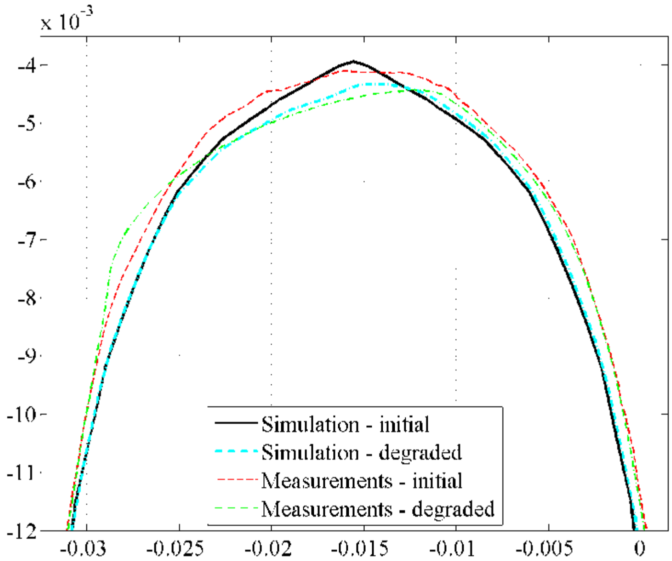

Figure 6. Measured and simulated crossing nose profiles at Haste before and after five weeks of mixed traffic. Dimensions in metres. From [4.2]

.

4.4. Conclusions and recommendations for future work

A methodology for the simulation of degradation of rail profiles in S&C has been developed. The methodology includes: simulation of dynamic vehicle–track interaction considering stochastic variations in input data, simulation of wheel–rail contacts accounting for non-linear material properties and plasticity, and simulation of wear and plastic deformation in the rail during the life of the S&C component. Two demonstration examples have been studied in this work: the switch panel of a turnout at Härad in Sweden, and the frog (crossing nose and wing rails) of a turnout at Haste in Germany. For the latter example, simulation results have been compared with measurements after five weeks of mixed traffic. Good qualitative agreement was found for the profile evolution of the crossing nose, which to some extent validates the simulation methodology. A number of possible parameter investigations can now be performed with the proposed simulation methodology: traffic situation (vehicle type, speed, axle load etc), switch geometry and material of switch components.

Only experimental data for the steel grades R260 and 350HT were available sufficiently early in the project to be used in the presented simulations. These steel grades are not used for the same S&C components and a comparison was therefore not relevant. The simulations have so far not been used to choose/optimise the steel grade. Instead the main result in this part of the project is the development of the simulation methodology itself. This methodology can be used in future work to choose/optimise steel grade when cyclic experimental data are available for these steel grades.

4.5. Bibliography

4.1 A Johansson, B Pålsson, M Ekh, J C O Nielsen, M K A Ander, J Brouzoulis, E Kassa, Simulation of wheel–rail contact and damage in switches & crossings, *Proceedings 8th International Conference on Contact Mechanics and Wear of Rail/Wheel Systems*, Florence, Italy, September 15-18, 987-996, 2009

4.2 D Nicklisch, J C O Nielsen, M Ekh, A Johansson, B Pålsson, A Zoll, J M Reinecke, Simulation of wheel–rail contact and subsequent material degradation in switches & crossings, *Proceedings 21st International Symposium on Dynamics of Vehicles on Roads and Tracks*, Stockholm, Sweden, August 17-21, 2009, 14 pages (available on CD)

5. Conclusions

A methodology for the simulation of degradation of rail profiles in S&C due to wear, accumulated plastic deformation and RCF has been developed. The methodology relies on that Low Cycle Fatigue (LCF) test data are available for a proper model calibration of the studied rail material. Such test data for rail material R350HT was available to allow for a numerical study where simulation results could be compared with field measurements after five weeks of mixed traffic over a crossing at Haste in Germany. Good qualitative agreement was found for the damage of the crossing nose, which serves as a validation of the simulation methodology.

Laboratory tests have been conducted to provide input data for the simulation tool and to give a better understanding of the behaviour of different materials in the examined load situations. The new database includes measured data for three materials commonly used in S&C: the bainitic steel B360, the austenitic steel Mn13 and the fine-pearlitic steel R350HT. For the fatigue tests in the laboratory, the materials were exposed to loads that were cycled either around zero stress or a mean tensile stress. For the monotonic tensile testing, the loading was in pure tension. It is recommended to perform additional tests in full-scale test rigs using compressive loading to identify other material properties that are crucial for a long life in S&C applications.

The main results delivered in this report are the material database and the development and validation of the simulation methodology. In future work, the methodology can be used for any given traffic situation (including a mix of different vehicle types, train speeds, axle loads) on a given switch geometry to choose steel grade and to optimise rail profiles.

6. Annexes

Appendix A in D3.1.6

A Johansson, B Pålsson, M Ekh, J C O Nielsen, M K A Ander, J Brouzoulis, E Kassa, Simulation of wheel–rail contact and damage in switches & crossings, *Proceedings 8th International Conference on Contact Mechanics and Wear of Rail/Wheel Systems*, Florence, Italy, September 15-18, 987-996, 2009

Appendix B in D3.1.6

D Nicklisch, J C O Nielsen, M Ekh, A Johansson, B Pålsson, A Zoll, J M Reinecke, Simulation of wheel–rail contact and subsequent material degradation in switches & crossings, *Proceedings 21st International Symposium on Dynamics of Vehicles on Roads and Tracks*, Stockholm, Sweden, August 17-21, 2009, 14 pages (available on CD)

Appendix C in D3.1.6

M Schilke, J Ahlström, Laboratory tests of material properties, *Department of Materials and Manufacturing Technology, Chalmers University of Technology*, Gothenburg, Sweden, 16 pages. See from next page

Appendix C in D3.1.6

Laboratory tests of material properties

witten by

Martin Schilke and Johan Ahlström
Department of Materials and Manufacturing Technology
Chalmers University of Technology
Gothenburg, Sweden.

1. Test methodology and remarks

Three different types of fatigue tests have been conducted:

1. Uniaxial strain controlled tests, symmetric around 0 (R_ε = -1), where the strain amplitude was held constant at 0.4%, 0.6% or 1.0%.
2. Uniaxial stress controlled tests, symmetric around 0 (R_σ = -1), where the stress amplitude was held constant at values corresponding to stress amplitudes recorded at half the number of cycles to failure in the strain controlled tests.
3. Ratcheting tests, performed in stress control with a positive mean stress to achieve an R-value of -0.8 ($R = \sigma_{\min} / \sigma_{\max}$).

During the tests the maximum and minimum values for stress and strain were logged for each load cycle. Full stress-strain (hysteresis) loops were logged with certain intervals depending on the expected number of cycles to failure (N_f).

Monotonic behaviour was compared to cyclic behaviour for the three materials. In these comparisons the monotonic stress strain curve was compared to the peak stress and peak strain amplitudes measured at the cycle constituting half the number of cycles to failure ($N_f/2$). This procedure must be kept in mind when judging the results for the Mn13 because it peaks well before $N_f/2$ and has already started to soften. Also the B360 has softened substantially at $N_f/2$.

Tensile tests were performed at two different strain rates, 10%/s and 0.01%/s at three different temperatures -60°C, 20°C and 100°C.

Repeatability for both fatigue and tensile tests was high which indicates that the batches of the different materials provided for testing were homogenous.

Hardness tests were performed according to ASTM E92 standard with HV30 for B360 and Mn13 and HV10 for 350HT.

Pictures and micrographs were taken with light-optical microscopy and scanning electron microscopy with EDX. The chemical composition was determined by Degerfors Laboratorium AB, Sweden.

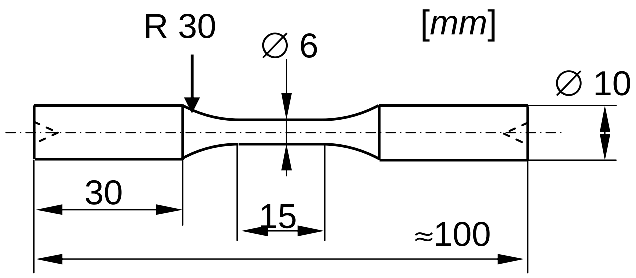

Figure A1. Geometry of tensile and fatigue test specimen

2. Chemical analyses

Table A2. Chemical composition in wt.-% (Measured by Degerfors LAB).

	B360	350HT	Mn13
C	0.316	0.79	1.14
Si	1.27	0.44	0.36
Mn	1.57	1.19	12.25
P	0.016	0.014	0.008
S	0.014	0.013	<0.001
Cr	0.55	0.08	0.18
Ni	0.03	0.02	0.12
Mo	0.15	<0.01	0.03
Ti	0.034	<0.003	0.003
Nb	<0.005	<0.005	0.017
Cu	<0.010	0.018	0.047
Co	0.005	<0.005	0.005
N	0.004	0.004	0.015
Sn	<0.005	<0.005	0.002
W	<0.01	<0.01	0.01
V	0.007	<0.005	0.005
Al	<0.002	<0.002	<0.002
Ta	0.01	0.009	0.024
Ca	<0.0005	<0.0005	0.0011
B	0.0003	<0.0002	<0.0002
As	<0.002	0.002	0.003
Fe	96	97.4	85.8

2. B360

2.1 Metallographic and hardness examinations

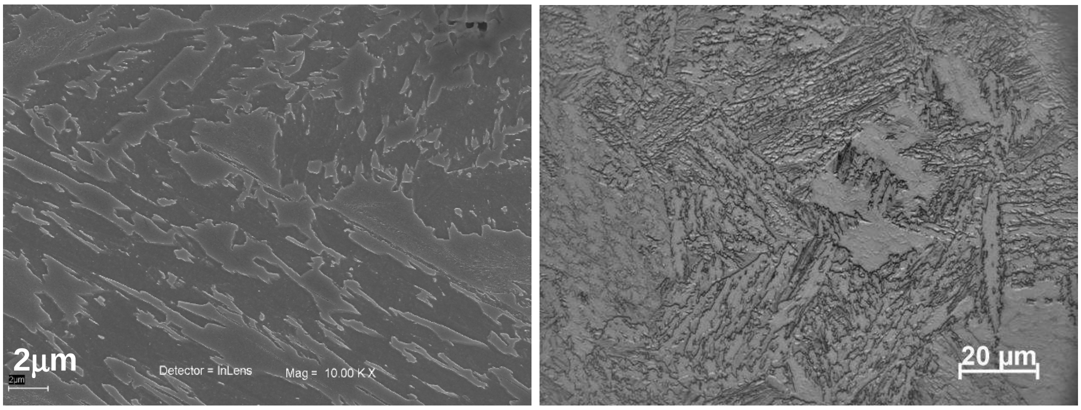

Figure A2. Micrographs of B360 in various magnifications taken in scanning electron microscope (left) and light optical microscope (right)

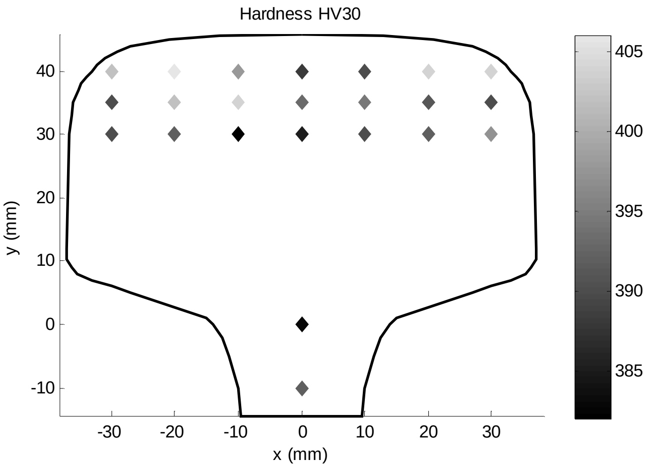

Figure A3. Hardness distribution of B360

The metallographic and hardness examination (Figure A2, Figure A3) of the B360 material shows an almost fully bainitic microstructure and uniform hardness distribution (Figure A3).

2.2 Tensile and fatigue tests

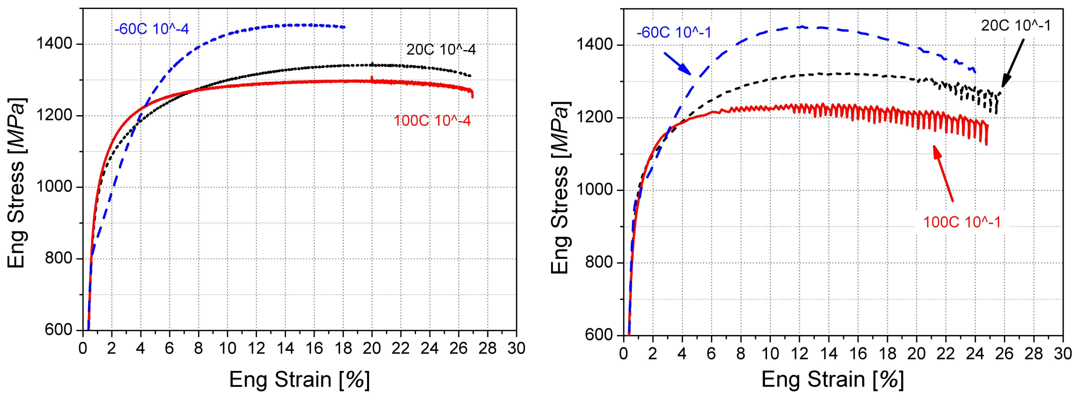

Figure A4. Tensile behaviour at three temperatures for strain rates of 0.01 % s^{-1} (left) and 10 % s^{-1} (right)

The tensile test results show rather strong temperature dependence. Compared to the room temperature behaviour, the hardening is weaker at 100°C and stronger at -60°C. The ultimate tensile strength increases with decreasing temperature as expected. The strain rate dependency is not very pronounced.

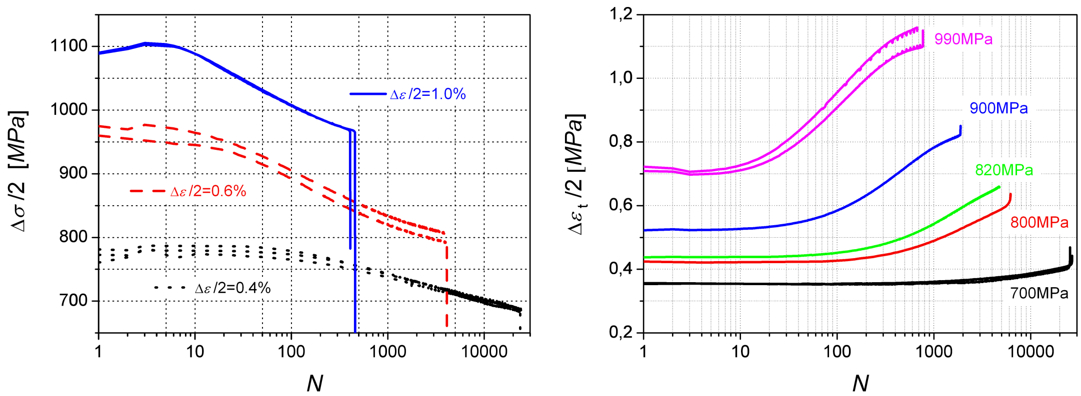

Figure A5. Stress (left) and strain (right) amplitude development during strain and stress controlled low cycle fatigue testing, respectively

Under strain controlled testing, B360 shows continuous softening throughout the fatigue life (Figure A5). The softening is stronger for the higher strain amplitudes. The stress controlled tests show similar behaviour with increasing strain amplitudes throughout the fatigue life due to material softening.

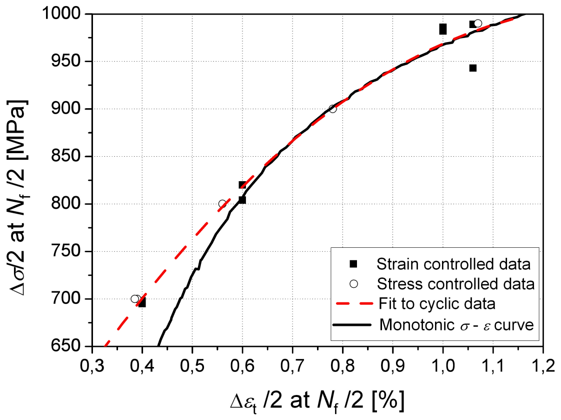

Figure A6. Comparison of cyclic and monotonic stress-strain curves

The hardening behaviour under cyclic strain and stress controlled testing is almost identical (Figure A6). The hardening behaviour of the material under cyclic and monotonic testing is similar.

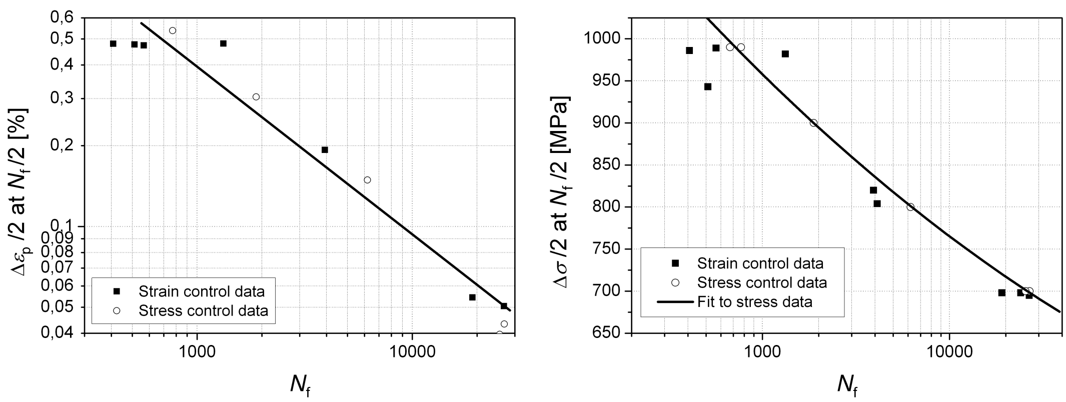

Figure A7. Coffin-Manson chart (left) and Wöhler chart (right)

The Coffin-Manson and the Wöhler charts (Figure A7) show the number of cycles to failure as a function of the load level. These types of diagrams are often used for dimensioning. Which diagram to choose depends on the loading situation, where the Wöhler chart is more suitable for force controlled loading situations and Coffin-Manson suits better for displacement controlled loading situations. The two graphs indicate similar results for stress and strain controlled tests. The scatter in number of cycles to failure is rather small except at the highest amplitudes.

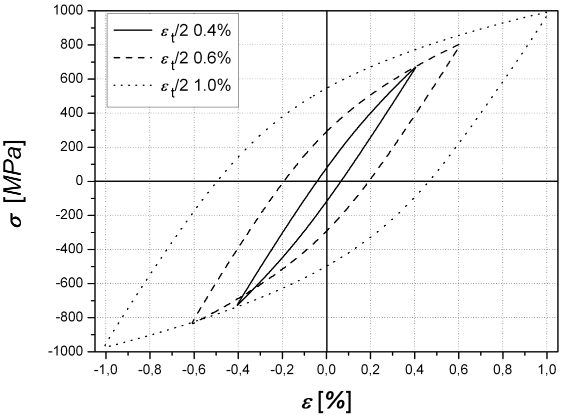

Figure A8. Hysteresis loops at $N_f/2$ in strain controlled tests

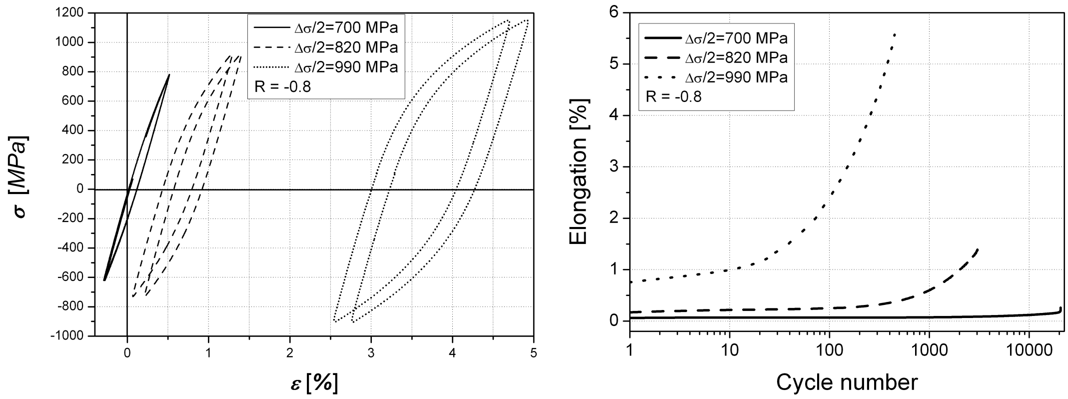

Figure A9. Hysteresis loops at $N_f/2$ for the ratcheting tests (left); elongation during the ratcheting tests (right)

Figure A8 and Figure A9 show hysteresis loops for different test conditions. Such recorded data have been used to calibrate material models.

3. R350HT

3.1 Metallographic and hardness examinations

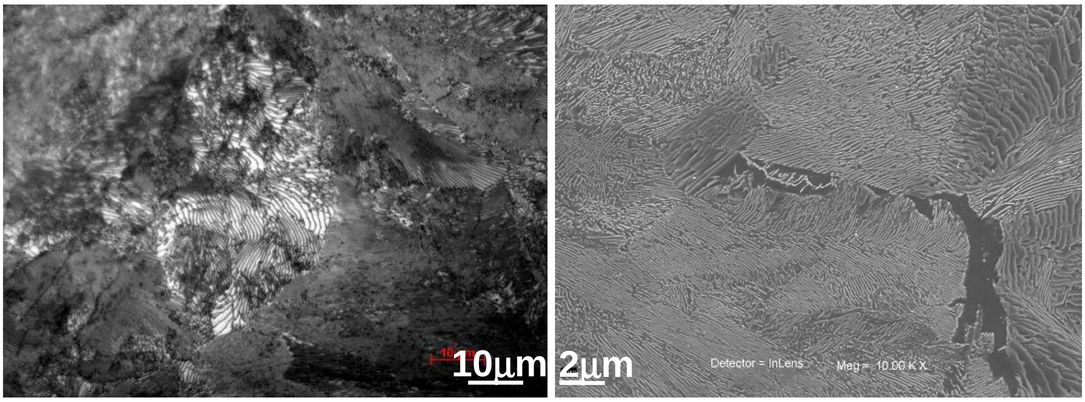

Figure A10. Micrographs of R350HT from light optical microscope (left) and electron microscope (right)

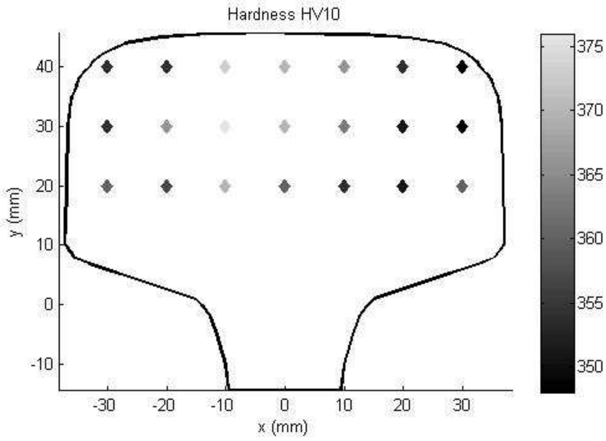

Figure A11. Hardness distribution of R350HT

Metallographic and hardness investigations demonstrate the R350HT as a fully pearlitic material (Figure A10) with a uniform hardness distribution (Figure A11).

3.2 Tensile and fatigue tests

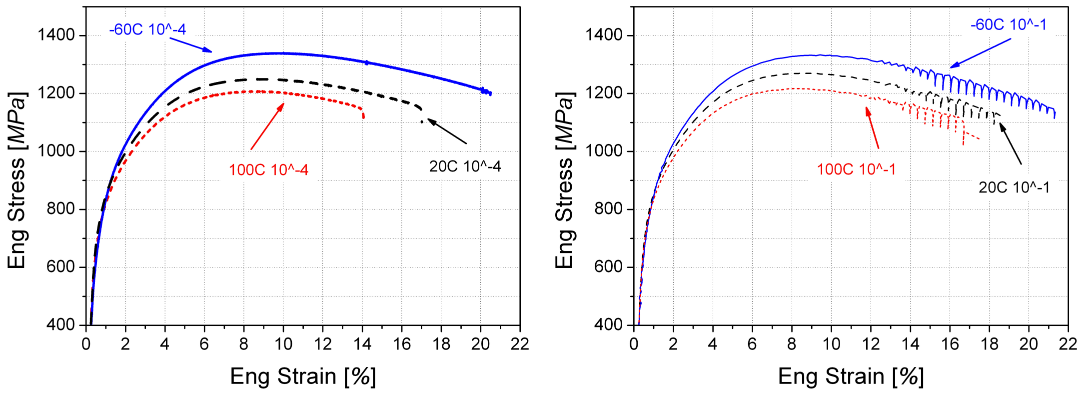

Figure A12. Tensile behaviour at three temperatures for strain rates of 0.01 % s^{-1} (left) and 10 % s^{-1} (right)

The tensile tests show some temperature dependence. The highest ultimate tensile strength is obtained for the lowest temperatures. Differences due to strain rates are small.

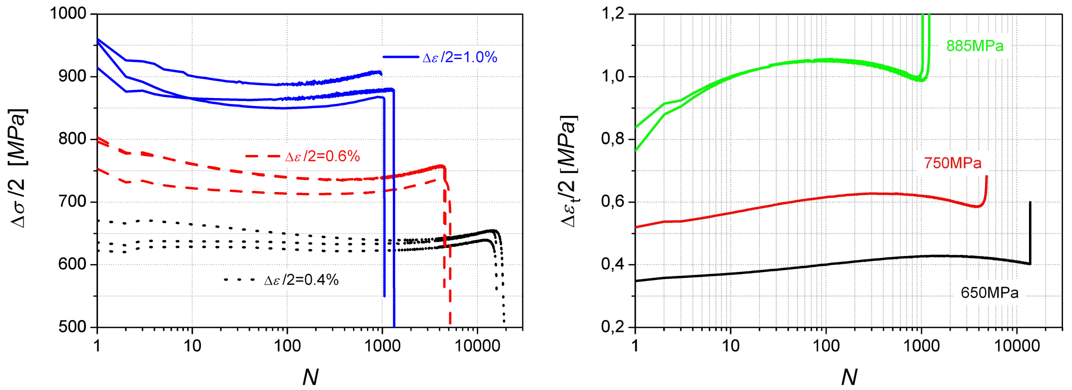

Figure A13. Stress (left) and strain (right) amplitude development during fatigue testing

During fatigue testing, 350HT softens slightly in the beginning of the test and then hardens gradually but not very pronounced until failure. This effect can be seen both for strain and stress controlled fatigue testing (Figure A13).

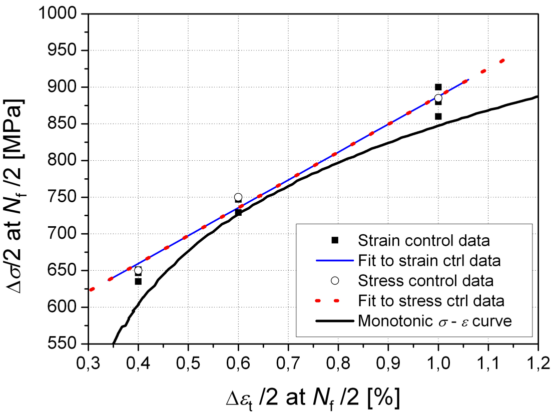

Figure A14. Comparison of cyclic and monotonic hardening

Hardening development under monotonic and cyclic loading is quite similar (Figure A14) and cyclic data seem independent of control mode.

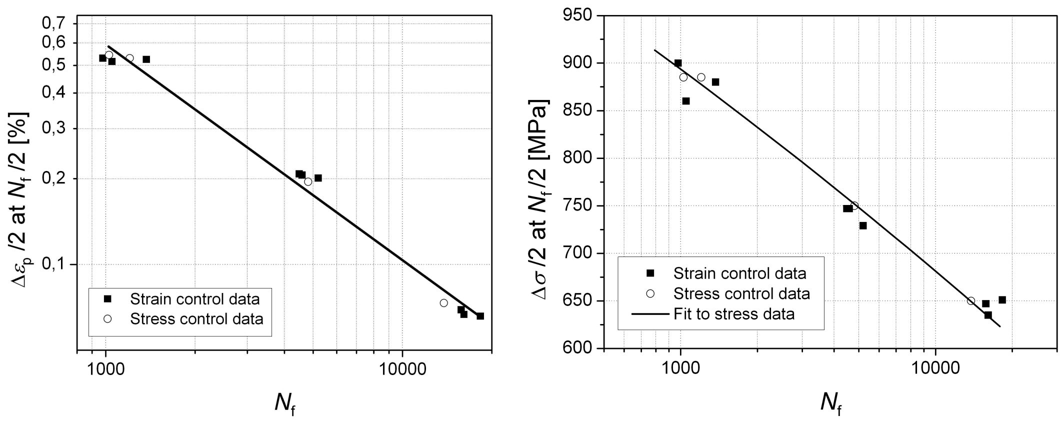

Figure A15. Coffin-Manson chart (left) and Wöhler chart (right)

Figure A15 shows small scatter in number of cycles to failure for all stress and strain amplitudes. As for the bainitic material, the results for stress and strain controlled tests are similar, i.e. the control mode used during testing does not influence the number of cycles to failure.

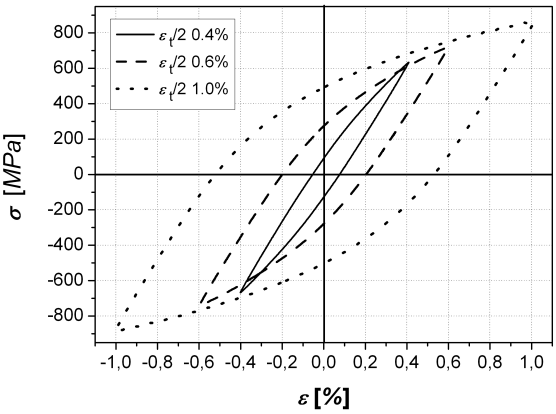

Figure A16. Hysteresis loops at $N_f/2$ in strain controlled tests

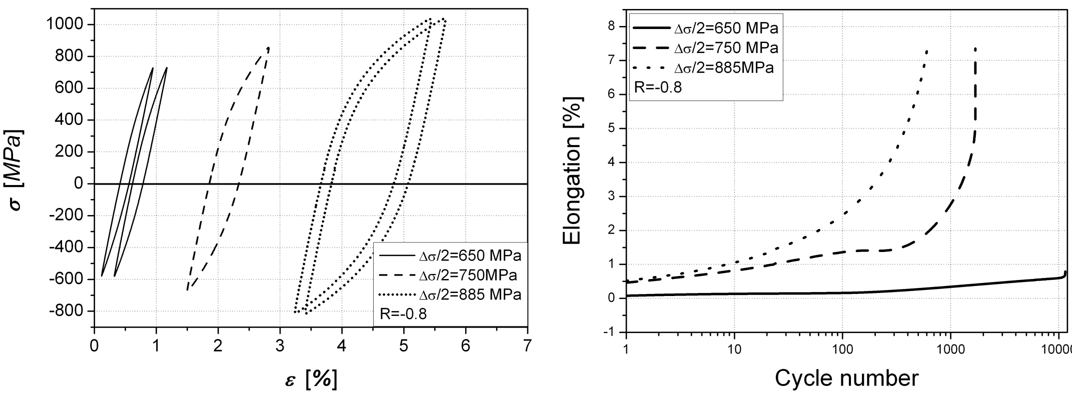

Figure A17. Hysteresis loops at $N_f/2$ for ratcheting tests (left); elongation during ratcheting tests (right)

4. Mn13

4.1 Metallographic and hardness examinations

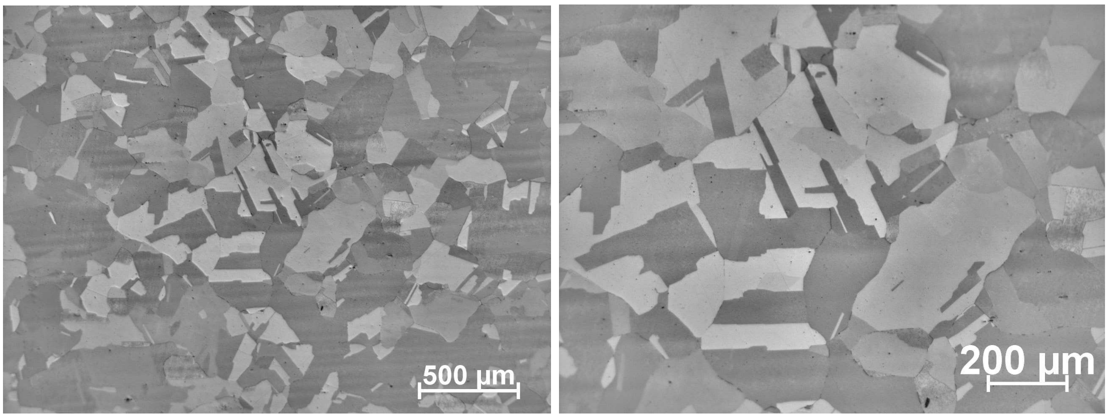

Figure A18. Micrographs of Mn13 taken in light optical microscope

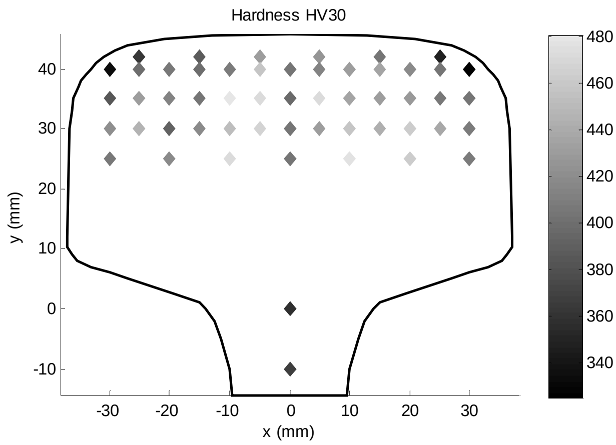

Figure A19. Hardness distribution of Mn13

The mechanical behaviour of Mn13 deviates from the other two materials imposing problems with test bar buckling in compression for the planned test setups. Stress controlled tests could therefore only be conducted at small stress amplitudes. Also ratcheting tests could only be performed at low stress amplitudes.

The metallographic examination of Mn13 reveals a fully austenitic microstructure with uniform grain sizes (Figure A18). Hardness measurements show differences of more than 100HV (Figure A19). The reason for this is not clear, but it could be related to the casting or rolling conditions. As the results from tensile and fatigue testing show, the repeatability is satisfactory despite the hardness variations in the virgin state. This is explained by the, in comparison to the other two materials, more pronounced plastic deformation and hardening the Mn13 material goes through, which means that the initial hardness of the material has almost no influence.

4.2 Tensile and fatigue tests

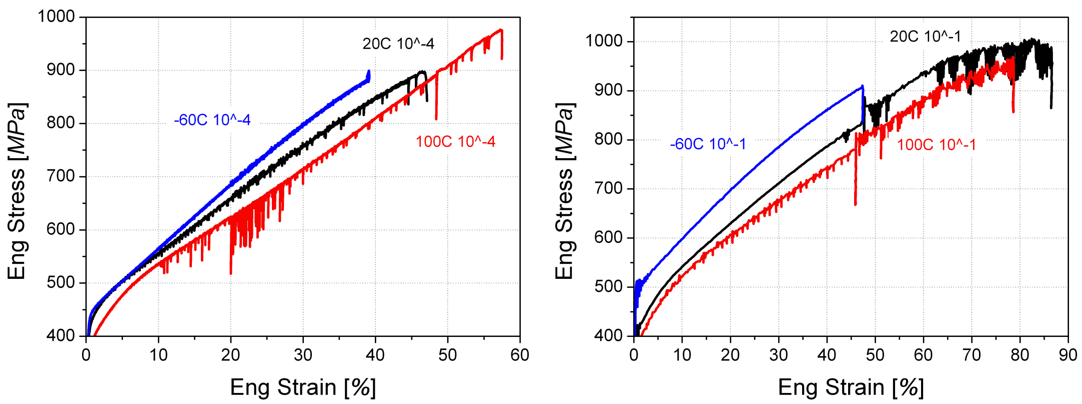

Figure A20. Tensile behaviour at three temperatures for strain rates of 0.01 % s^{-1} (left) and 10 % s^{-1} (right)

In tensile testing temperature effects are not very pronounced as expected for an austenitic material. The strain rate however seem to influence the elongation to rupture. With a higher strain rate the elongation increases significantly especially at medium and high temperature (Figure A20).

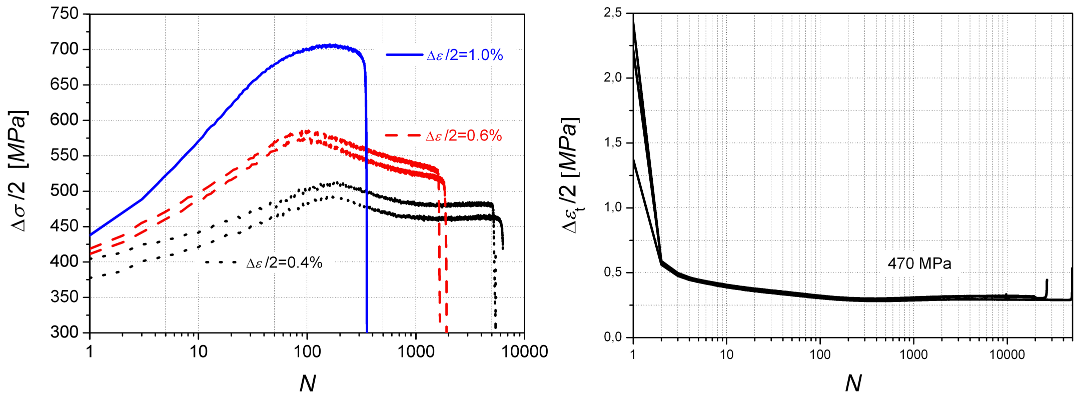

Figure A21. Stress (left) and strain (right) amplitude development during fatigue testing

The strain controlled tests show pronounced hardening of the Mn13 in the beginning of the test followed by softening (Figure A21). At high strain amplitudes the softening is not as pronounced. The stress controlled tests show a massive hardening in the very first couple of cycles followed by relative stability for the remainder of the test. The reason is that the strong hardening eliminates further plastic straining which results in a close to elastic response. This also leads to increased number of cycles to failure in the stress controlled tests.

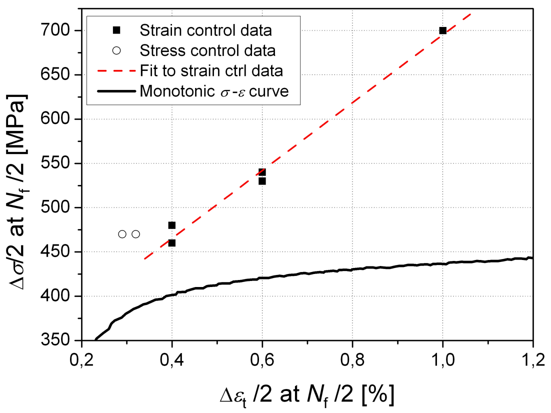

Figure A22. Comparison of cyclic and monotonic hardening

Mn13 shows a more pronounced hardening under cyclic fatigue loading than under monotonic tensile testing.

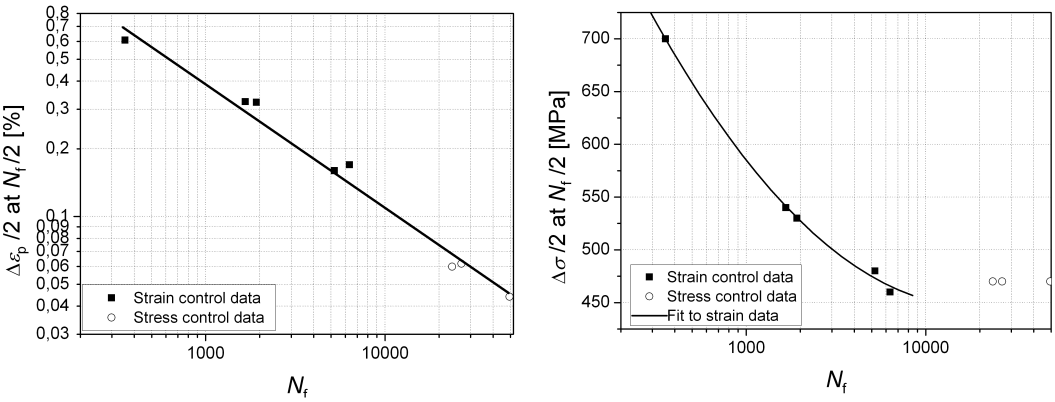

Figure A23. Coffin-Manson chart (left) and Wöhler chart (right)

The Wöhler chart shows that for this material there is a large dependency on the loading condition. This type of diagram should ideally be produced by stress controlled tests which means that the diagram should be taken as indicative as it contains only one stress amplitude level. For the other materials in the study the situation has been different.

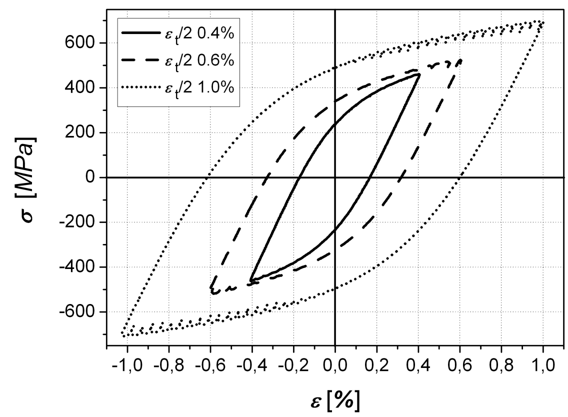

Figure A24. Hysteresis loops at $N_f/2$ in strain controlled tests

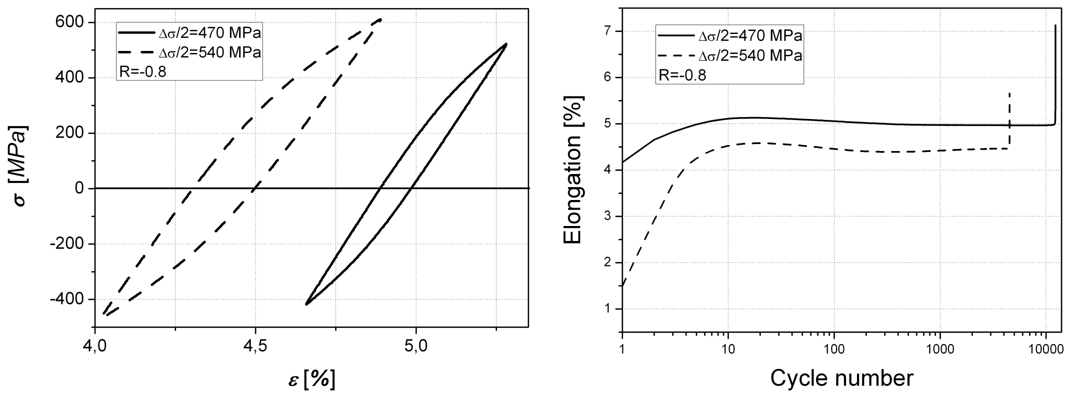

Figure A25. Hysteresis loops at $N_f/2$ for the ratcheting tests (left); elongation during ratcheting tests (right)